J. Fluid Mech. (2020), *vol.* 892, A36. © The Author(s), 2020.
Published by Cambridge University Press
doi:10.1017/jfm.2020.192

Surfing of drops on moving liquid–liquid interfaces

Teng Dong[1], **Fei Wang**[1,2], **Weheliye H. Weheliye**[1] **and Panagiota Angeli**[1,†]

[1]ThAMeS Multiphase, Department of Chemical Engineering, University College London, London WC1E 7JE, UK

[2]Beijing Institute of Space Long March Vehicle, No. 1 Nandahongmen Road, Fengtai District, Beijing 100076, PR China

(Received 2 August 2019; revised 25 December 2019; accepted 5 March 2020)

The delayed coalescence of drops with the interface between a moving aqueous layer and an oil phase is investigated in a novel flow channel. Drops are released onto oil–aqueous interfaces moving at velocities from 0 cm s^{-1} up to 3.4 cm s^{-1}. The evolution of the drop shape, the film thickness between the drop and the bulk liquid, and the velocities of the drop surface and the bulk interface were measured with planar laser-induced fluorescence. As the interface speed increases, the drop coalescence is delayed. This is attributed to the lubrication pressure that develops in the draining film. This pressure was calculated by using the drop shape and the tangential velocities of the drop surface and the bulk interface, and was shown to increase with the interface velocity. The film forming between the drop and the bulk liquid has a dimple shape, symmetric about the centreline. With increasing interface velocity, the dimple shifts to the front part of the drop, resulting locally in a low pressure, which leads to film rupture. As the film breaks, 'oil drops on a string' formations are entrained into the water phase, which is rarely seen when a drop coalesces with a stationary liquid–liquid interface. The velocity fields in the drop were investigated with particle image velocimetry. It is found immediately after reaching the interface that the drops accelerate to reach the interface speed. Initially there is a strong internal circulation in the drops, which decays quickly as the drops approach the speed of the interface.

Key words: drops, breakup/coalescence, multiphase flow

1. Introduction

When a liquid drop falls on the surface of its homophase, coalescence is expected to occur (Charles & Mason 1960; Klyuzhin *et al.* 2010). Coalescence of drops is ubiquitous in nature as well as in industrial applications such as transportation of oil mixtures with water (Venkataraman *et al.* 2013; Farhadi *et al.* 2016), milk processing (Tcholakova *et al.* 2006), spray painting (Dalili *et al.* 2017) and drug encapsulation (Andrade *et al.* 2015). In some applications, such as oil–water separation (Kavehpour 2015), rapid coalescence is desirable, while in other areas, including the food,

† Email address for correspondence: p.angeli@ucl.ac.uk

pharmaceuticals and cosmetics industries (Jafari *et al.* 2008; Deng *et al.* 2016; Muijlwijk *et al.* 2017), coalescence should be prevented to maintain the stability of emulsions. In some cases, the drops rest on the liquid surface for a long time before they coalesce. As early as 1881, Reynolds discussed this phenomenon and indicated that impurities of the surface might lead to coalescence (Reynolds 1881). In contrast, later studies found an increase of the drop rest time when detergents or surfactants were added (Yeo & Matar 2003; Dai & Leal 2008; Dong *et al.* 2017; Dong, Weheliye & Angeli 2019). In fact, surfactants are widely used to stabilize emulsions or dispersions (Sajjadi, Zerfa & Brooks 2002; Li, Zhang & Thoroddsen 2013).

Delay of drop coalescence with an interface can also be achieved by other means. Previous research by J. A. Raymond, as reported by Walker (1978), showed that mechanical vibrations were able to increase the rest time of drops on a liquid surface for as long as 18 min. In a similar experiment, Walker (1978) tested the delayed coalescence of drops on an oscillating plate at 10–150 Hz, and found that oscillations in the middle of the amplitude range resulted in the longest drop rest time, while a smaller or larger amplitude reduced the drop life. When a drop approaches the interface of its homophase with air, a thin film of air is trapped and coalescence occurs when the thin film drains out. Accordingly, Walker (1978) attributed the delay of coalescence to the refill of the air film as a result of the vibrations. The refill mainly happens with small drops (Couder *et al.* 2005). With large drops, vibrations are dampened, and the drainage of the air film is delayed. Vibrating interfaces have recently been used to delay the coalescence of drops (Couder *et al.* 2005; Damiano *et al.* 2016; Pucci *et al.* 2018; Sáenz, Cristea-Platon & Bush 2018). Moláček & Bush (2013) combined the properties of the fluids and the vibration parameters of the interface in a map of drop behaviour, which included coalescence, bounce, walk and chaotic behaviour. Sáenz *et al.* (2018) recently discovered a statistically well-defined pattern of the speed of the floating drops on vibrating surfaces. More specifically, they found that, under their experimental conditions, the velocity distribution resembled a series of concentric annuli.

A temperature difference between the drop surface and the interface can delay coalescence as well. For example, a temperature difference of $\Delta T = 30\,^{\circ}\mathrm{C}$ between two drops of 5 cSt silicone oil can delay coalescence for 1 h until ΔT reduces below a critical value of $\Delta T_c = 3.0 \pm 1.0\,^{\circ}\mathrm{C}$ (Dell'Aversana, Banavar & Koplik 1996). Geri *et al.* (2017) found that the delay increased monotonically with the initial temperature difference ΔT_0. The thermally induced Marangoni effect was considered to be responsible for preventing coalescence in such cases (Napolitano, Monti & Russo 1986). The magnitude of the thermally induced Marangoni flow is characterized by the velocity $v_m = \sigma_T \Delta T/\mu$ (Dell'Aversana *et al.* 1996; Savino, Paterna & Lappa 2003), where σ_T is the interfacial tension corresponding to temperature T, ΔT is the temperature difference and μ is the dynamic viscosity of the liquids. According to the lubrication theory, the pressure that resists coalescence is estimated to be equal to $\Delta P = \mu_a \sigma_T R \Delta T/(\mu_p h^2)$, where μ_a and μ_p are the viscosity of the air and the bulk liquid pool, and h is the thickness of the trapped air film (Savino *et al.* 2003). By equating the lubrication pressure over the drop to the weight of the drop, Davanlou (2016) correlated the film thickness at equilibrium to the temperature gradient for the drop to float upon a liquid pool, $h = \sqrt{3\sigma_T \mu_a \Delta T/(16\rho_d g \mu_p)}$. According to the equation, an increase in temperature difference leads to a thicker air film.

Dell'Aversana *et al.* (1996) suggested that the main reason for the delay in coalescence of drops with moving bulk liquid layers of the same phase, compared to

stationary ones, is the change in the tangential velocities along the drop surface and the bulk liquid interface. The modified tangential velocities increase the lubrication pressure while they help the surrounding fluid to be entrained in the film, thus resisting the contact of the drop with the bulk liquid homophase. They found that a drop can float on a moving interface in the absence of a temperature gradient. The phenomenon was confirmed by subsequent works (Sreenivas, De & Arakeri 1999; Lhuissier *et al.* 2013). Sreenivas *et al.* (1999) investigated the non-coalescence of drops at the hydraulic jump of a flowing film. It was, however, shown that the drops do not always stay at the hydraulic jump steadily but oscillate (Pirat *et al.* 2010), which is not conducive to the study of the dynamics of the trapped film. Similarly, steady drop floating was achieved by releasing drops on the inner surface of a rotating cylinder coated with a thin layer of the same liquid as in the drop (Davis, Dransfield & Tan 1980; Thoroddsen & Mahadevan 1997; Lhuissier *et al.* 2013; Sawaguchi *et al.* 2019). Whether the drops can levitate on the surface or not depends a lot on the impact conditions. A phase map was plotted by Castrejón-Pita *et al.* (2016) to indicate the different patterns using $We\,Re^{1/2}$ and $v_t/(v_n Re^{1/2})$ as coordinates, where *We* and *Re* are the Weber and Reynolds numbers, and v_t and v_n are the velocity of the surface and the impact velocity of the drop. Drop levitation was observed on the liquid surface at large values of $v_t/(v_n Re^{1/2})$, which requires a high viscosity of the liquids, a low impact velocity and a large rotation speed. Through direct observation, Davis *et al.* (1980) found that the shape of the floating drop is affected by the rotation speed of the cylinder: a flatter bottom of the drop could be produced at higher speeds.

The rest time of drops on a moving liquid surface depends on two parameters, the thickness and the pressure in the film that separates the drop from the interface. Lhuissier *et al.* (2013) used interferometry and found that, when drops were levitated at the inner surface of a cylinder, the distribution of the film thickness was uneven. Using lubrication theory, the air film thickness was estimated, and was found to be partially in agreement with the measurements. For large drops, the film thickness is $h \sim Ca^{2/3}\kappa_b^{-1}$, while for small drops it is $h \sim Ca^{4/5}(a\kappa_b)^{4/5}\kappa_b^{-1}$, where the capillary number Ca is based on the velocity of the air film, κ_b is the surface curvature at the bottom of the drop and $a = (\sigma/\rho g)^{1/2}$ is the capillary length. According to the predictions, the film thickness increases with the air film velocity at a higher rate for small drops. Sawaguchi *et al.* (2019), in similar measurements, found that the thickness of the air film was evenly distributed at the bottom of low-viscosity drops, while large oscillations were observed for high-viscosity drops.

Sreenivas *et al.* (1999), who studied the levitation of drops at a hydraulic jump, suggested that the force needed to balance the weight of the drop was $W = f_L \mu_a v L_y L_x^2/h^2$, where v is the velocity of the trapped film, L_x and L_y refer to the length and width of the drop as it is deformed, and f_L is related to the shape factor L_x/L_y and inclination of the drop. However, no calculated results were given. Based on the lubrication theory, Sawaguchi *et al.* (2019) found the two-dimensional pressure distribution in the trapped film for a steadily floating drop. As the drop shape is controlled by the balance between the inner pressure of the drop given by the weight, the outer pressure in the film and the Laplace force, the film pressure can also be calculated if the local drop surface curvature is known. The results obtained from the two methods were in good agreement for most of the film apart from the small region at the exit of the film.

In many industrial applications where the drop is levitated over an interface, including oil petroleum transportation and oil–water separation (Rommel, Blass &

Meon 1993), the drops are surrounded by another liquid and the fluid interface is significantly deformed when the drop approaches it because of gravity. In most of the previous investigations, drops were generated in air and approached the interfaces of liquid films with air (Lhuissier *et al.* 2013; Castrejón-Pita *et al.* 2016; Sawaguchi *et al.* 2019). In such cases, drop levitation can be realized only when the interfaces have high speed and the liquids have large viscosity. In addition, as the liquid films were thin and close to the bottom wall, the interfaces were not significantly deformed. Lee *et al.* (2013) studied the lubrication phenomenon in the air layer between the curved jet of non-Newtonian liquids with greatly deformed surfaces. For other investigations, such as a drop levitated at the hydraulic jump of a film flow (Sreenivas *et al.* 1999), wakes were observed in the vicinity of the drops while the drops were oscillating during the levitation (Pirat *et al.* 2010). Recently, Hale & Akers (2016) investigated drop deceleration on a stationary liquid surface. However, in this case surfactants were used, and the delayed coalescence could be due either to the presence of the surfactants or to the relative motion between the drop and the bulk liquid.

In the previous studies, drop surfing and delayed coalescence were investigated on liquid surfaces with air. In many applications, however, drops coalesce with liquid–liquid interfaces and their surfing has not been studied. In this present study, a novel flow channel was designed, which allowed an oil–aqueous interface to move at different speeds as an aqueous drop was released on it. High-speed planar laser-induced fluorescence (PLIF) and particle image velocimetry (PIV) were used to obtain the shapes of the drop and the interface, the shape and thickness of the film trapped between the drop and the bulk liquid, and the velocities of the drop surface and the bulk interface bounding the film. The rest times of the drop on the interfaces are measured and the mechanism of delayed coalescence is discussed based on the lubrication pressure in the film and its dependence on the film shape and on the velocities of the drop bottom surface and of the bulk liquid interface. The changes of the drop shape at the initial stages of drop impact and rebound on the interface, as well as the acceleration of the drop immediately after the impact with the interface, are analysed. Lastly, new observations on the shape of the ruptured film and on entrainment of oil in the water phase are presented.

2. Experiment design and methodology

2.1. *Experimental set-up and materials*

The experimental set-up for the investigation of the delayed coalescence of drops with a liquid–liquid interface is shown in figure 1(*a*). A rectangular flow channel with a 5 cm × 5 cm cross-section and 1 m length was built for the tests. The flow channel was connected to an inlet chamber and an outlet chamber through two openings at 5 mm above the bottom wall, as shown in figure 1(*b*). Initially, an aqueous phase of glycerol solution in water (density $\rho_d = 1210$ kg m^{-3}, viscosity $\mu_d = 54$ mPa s^{-1}) was introduced into the channel by a Cole-Parmer® magnetic drive centrifugal pump. The pump was stopped and the valves were closed to hold the liquid in the channel with a surface height approximately equal to 15 mm from the bottom. The organic phase (Exxsol D80 oil, density $\rho_o = 804$ kg m^{-3}, viscosity $\mu_o = 1.75$ mPa s^{-1}) was then added into the channel through an oil inlet at 10 cm away from the outlet. The thickness of the oil film was set at approximately 20 mm. A flat stationary interface (interfacial tension $\sigma = 26.73$ mN m^{-1}) formed in the flow channel. The volume concentration of the glycerol was set at 78 % to match the refractive index of the

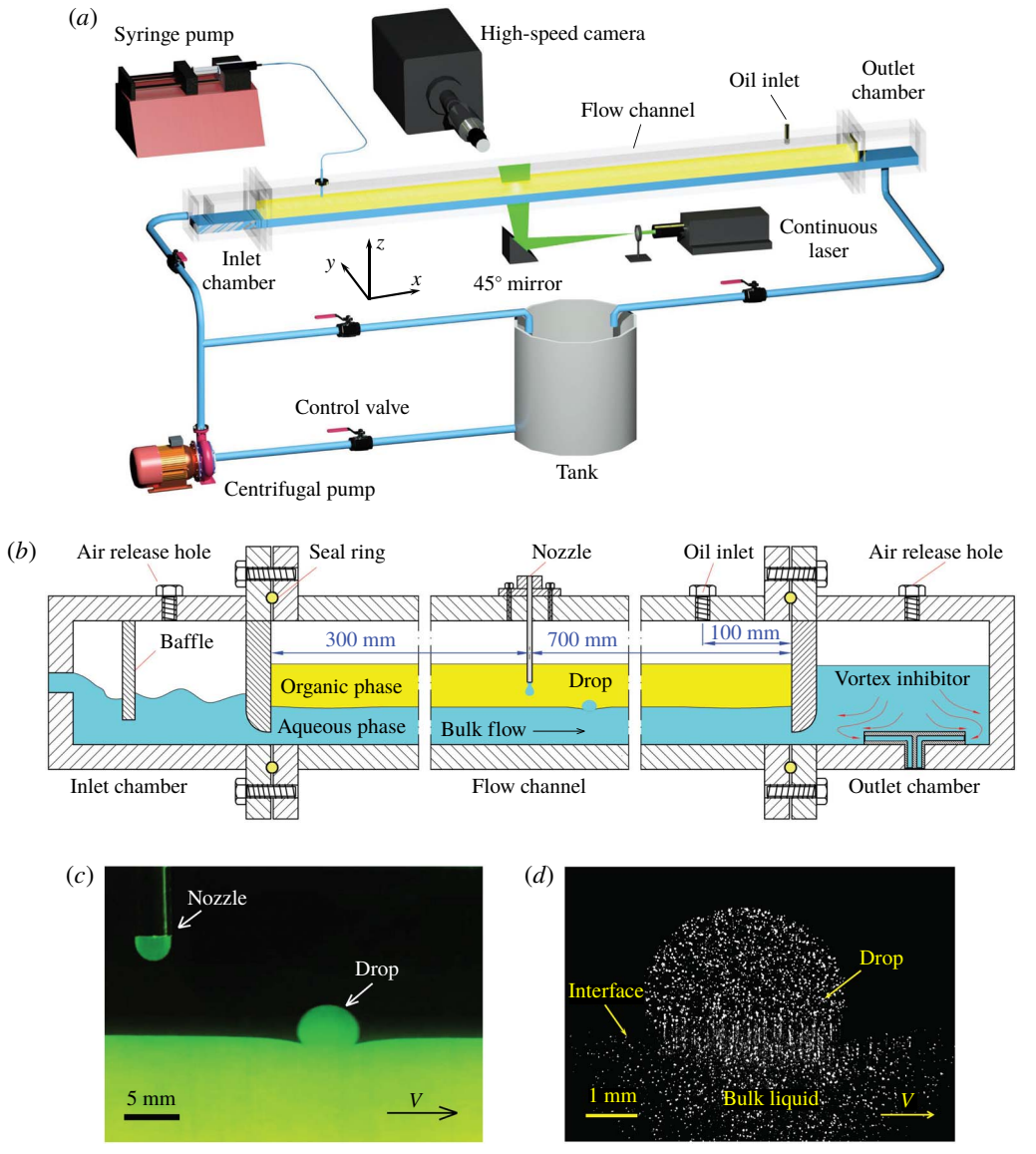

FIGURE 1. (*a*) Schematic of the experimental set-up. (*b*) Design details of the main flow channel along with the inlet chamber and the outlet chamber. (*c*) Image of the PLIF tests showing the nozzle position for delivering the drops. (*d*) Typical PIV raw image showing a drop surfing on the interface.

Exxsol D80 oil ($r_{ref} = 1.443$ at 20 °C) and prevent light aberration at the interface in the optical experiments. The refractive indices of the fluids were measured with an Abbe 5® refractometer.

Subsequently, the valves were opened and the pump was restarted to circulate the 78 % glycerol solution in the channel. Because of the motion of the water phase, the interface was also set in motion. As shown in figure 1(*b*), a baffle was placed opposite the aqueous-phase inlet to dampen any disturbances on the flat interface.

In addition, the bottom of the wall that separated the inlet chamber from the main channel had a smooth shape to reduce any waves at the interface. In the outlet chamber, a cross-shaped obstacle was placed in the drain hole to prevent any vortices forming. In the experiments, the interface speed was varied by changing the flow rate of the aqueous phase through the centrifugal pump. A rotameter with a maximum flow rate at 1 l min^{-1} with 5 % accuracy was installed in the inlet tube to monitor the flow rate.

As shown in figure 1(*b*), the aqueous-phase drops were generated by supplying the fluids from a syringe to a flat-ended nozzle that was located 30 cm away from the inlet. The flow rate in the nozzle was controlled by a programmable Aladdin® syringe pump and was set at 0.2 ml min^{-1}. The inner diameter of the nozzle is 2 mm, which produces drops of an average size of 5 ± 0.15 mm. As mentioned by Klyuzhin *et al.* (2010), the drop rest time, which is the difference between the time that the drop contacts the interface and the coalescence time, could be affected by the height of the nozzle from the interface. It was also found that the rest time was reduced when the nozzle was closer to the interface. The height of the nozzle was set at 10 mm above the interface for all tests, as shown in figure 1(*c*). To decide upon the design of the experimental set-up, some computational fluid dynamics simulations were carried out initially, which showed that for the aqueous-phase velocities used there was a weak circulation of the oil phase in the upper part of the channel. Placing the nozzle at 10 mm above the interface avoids the effect of the backflow on the drops. In addition, it was found from the simulations that the flow of the two phases reaches steady state in approximately 40 s. In the experiments, several drops were released and measurements were taken when the drops were found to move at a constant speed on the interface. For brevity in what follows, the drop interface is called the drop surface while the liquid–liquid interface between the oil and the aqueous bulk phases is called the (bulk) interface.

2.2. *Experimental methodology*

The rest times of the drops on the interface moving at different speeds were initially measured to evaluate the delay in coalescence. The falling time of the drops from the nozzle to the interface at the beginning and the coalescence time at the end were neglected, as they were very short compared to the rest period. A stopwatch with an accuracy of 0.01 s was used to measure the rest times. It was previously found that approximately 50 runs were sufficient to capture the distribution of the rest times of the drops with a stationary interface (Dong *et al.* 2017, 2019). In the current experiments, approximately 200 runs were conducted for each set of conditions to reduce uncertainties caused by the moving interface.

High-speed PLIF was then utilized to visualize the motion of the drop and the shape of the film, as was also shown by Oldenziel, Delfos & Westerweel (2012). The PLIF system consists of a Laserglow® continuous-wave laser (532 nm, 3 W) placed below the flow channel, which emits a laser beam with 4 mm diameter (see figure 1*a*). A spherical lens and a cylindrical lens were connected to the head of the laser in series to create a 1 mm thick laser sheet, which was directed to the flow channel by a 45° angle mirror. As the drop was generated in the middle of the channel in the y direction and no appreciable deviation from the centre was observed when it travelled with the interface along the x direction (see figure 1*c*), the middle plane of the drop could be illuminated when it went through the laser plane. A small amount of the fluorescent dye Rhodamine 6G was dissolved in both the drop and the aqueous film

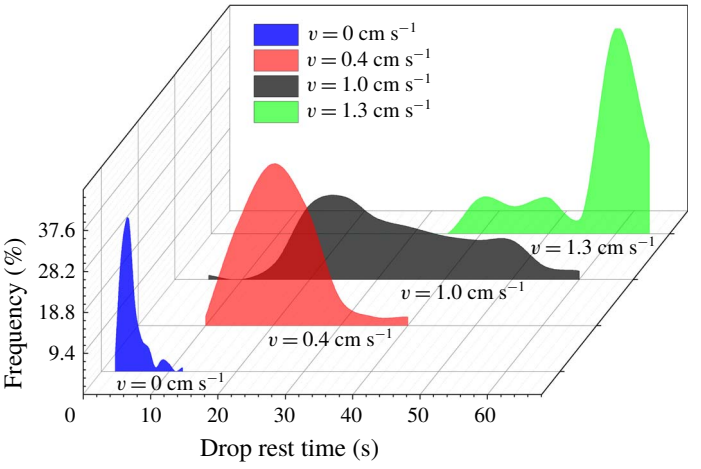

FIGURE 2. Probability distribution of drop rest time at the liquid–liquid interfaces with different speeds.

to help distinguish the interfaces and the structure of the oil film trapped between the drop and the bulk interface. A Phantom® V1212 high-speed camera, equipped with a mono-zoom Nikkon lens, which gave a spatial resolution of 14 μm pixel^{-1}, was placed perpendicular to the laser sheet to capture the whole process. Since it was quite challenging to track the motion of the drops by moving the high-speed PLIF system, the laser plane and the high-speed camera were located at different distances up to 20 cm away from the location of the drop impact onto the interface. The frame rate of the high-speed camera was set at 1000 frames per second to record clear images at each instant. The PLIF video showing the drop travelling along the interface from the impact position is given as Movie 1 in the supplementary movies available online at https://doi.org/10.1017/jfm.2020.192.

The velocity fields in the drop were also studied with PIV. For these measurements, the drops were seeded with 1 μm Rhodamine-coated spherical particles. A typical PIV raw image of an aqueous drop close to the oil–aqueous interface is shown in figure 1(*d*). As the size of the droplet is larger than the thickness of the laser sheet, the drop surface curvature should not affect the measurements. The open-source freeware JPIV was used to post-process the images obtained from the camera through the adaptive correlation tracking of the full image with a final interrogation window of 32×32 pixels. A 50 % window overlap was used for a final resolution of 16×16 pixels, corresponding to an area of 0.2 mm $\times$ 0.2 mm.

3. Delayed coalescence and lubrication model

The experiments showed that drop coalescence is significantly delayed when the oil–water interface is moving. Figure 2 shows the probability distribution of the drop rest times at interfaces of different speeds. When the interface is stationary, most of the drops break in less than 10 s with a peak coalescence time at approximately 4 s. When the interface is moving, however, an increase of the drop rest time is observed. At an interface speed of $v = 0.4$ cm s^{-1}, the drop rest time presents a normal distribution, while no drop was found to coalesce in less than 10 s. Compared to the distribution with stationary interfaces, the peak shifts to approximately 20 s. When

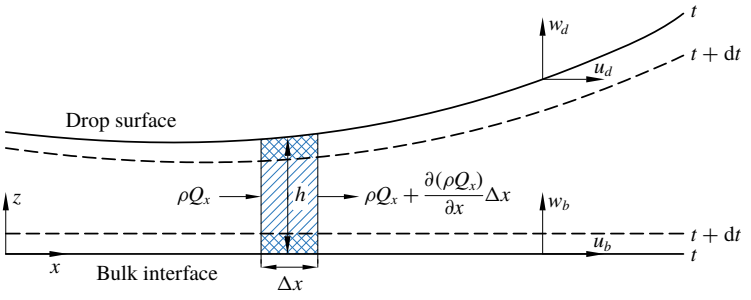

FIGURE 3. Schematic of the mass conservation in the control volume (hatched area) in the thinning film.

the speed of the interface reaches $v = 1.0$ cm s^{-1}, the distribution of the drop rest time becomes wider than the former two at $v = 0$ and $v = 0.4$ cm s^{-1}; some of the drops survive until 60 s, while a few break in less than 10 s. At $v = 1.3$ cm s^{-1}, the rest time shows a multimodal distribution, with three peak values located at various times. Despite this, however, the rest time is greatly increased compared to that at $v = 1.0$ cm s^{-1}. For many of the drops at $v = 1.3$ cm s^{-1}, coalescence does not happen within the channel. As these cases are not included in the statistical analysis, a sharp decrease is seen after the peak.

The coalescence of drops with liquid–liquid interfaces is complex and can be influenced by many factors (Chan, Klaseboer & Manica 2011), which explains the deviations of the rest time distributions from the normal one. Figure 2 clearly shows that coalescence is significantly delayed when the interface speed is increased. This is attributed to the lubrication pressure that develops in the film between the drop and the bulk interface, which resists the settling of the drop (Hamrock, Schmid & Jacobson 2004). As will be discussed in the following section, after the initial impact and rebound on the interface, the released drop moves forwards under the influence of the moving interface. After the drop rebounds, the Reynolds number of the draining film, $Re = \rho_o u h/\mu_o$, is lower than 1, where h and u refer to the film thickness and the velocity of the film liquid. Thus the inertial term in the Navier–Stokes equations can be considered negligible (Geri *et al.* 2017; Nakayama 2018; Sawaguchi *et al.* 2019). During the drop impact and rebound, Re might be close to 1 because the film is thick and the inertia of the film fluid should not be ignored. However, according to Sambath *et al.* (2019), the inertia of the film liquids has little effect on the impact dynamics compared to the liquid in the drop. The corresponding two-dimensional momentum equation for the lubrication film can be reduced to

$$\frac{\partial p}{\partial x} = \mu \frac{\partial^2 u}{\partial z^2}. \tag{3.1}$$

As shown in figure 3, a two-dimensional control volume with a unit width in the direction perpendicular to the x–z plane is taken into consideration with the boundary conditions $z = 0$ and $u = u_b$ at the bulk interface and $z = h$ and $u = u_d$ at the drop surface. According to Leal (2007), one of the two interfaces, the bottom bulk interface, is assumed to be flat to simplify the model. By integrating equation (3.1) with the boundary conditions, the velocity in the film is found to be equal to

$$u = -z\left(\frac{h-z}{2\mu}\right)\frac{\partial p}{\partial x} + u_b\left(\frac{h-z}{h}\right) + u_d\frac{z}{h}, \tag{3.2}$$

where u_d and u_b are, respectively, the velocities along the drop surface and the interface in the film region, with thickness h. Considering mass conservation, the rate of mass change in the control volume is equal to the difference between the mass rate flowing into and leaving the control volume, that is,

$$-\frac{\partial(\rho Q_x)}{\partial x}=\frac{\partial(\rho h)}{\partial t}, \tag{3.3}$$

where Q_x is the volume flow rate per unit width $Q_x=\int_0^h u\,\mathrm{d}z$. In the current experiments, the liquid in the film is incompressible and the density ρ is constant. The right-hand side of (3.3) can then be written as

$$\frac{\partial h}{\partial t}=w_d-w_b-\frac{\partial h}{\partial x}u_d, \tag{3.4}$$

where w_d and w_b represent the approaching velocities of the drop surface and the bulk interface. By substituting (3.4) into (3.3), the pressure distribution in the film is expressed as

$$\frac{\partial}{\partial x}\left(\frac{h^3}{12\mu}\frac{\partial p}{\partial x}\right)=\frac{\partial}{\partial x}\left(\frac{h\,(u_d+u_b)}{2}\right)+(w_d-w_b)-u_d\frac{\partial h}{\partial x}. \tag{3.5}$$

According to (3.5), the lubrication pressure in the film can be generated by (i) the variation of the film thickness, (ii) the interface velocity along the flow direction, and (iii) the approaching speed of the two interfaces. For coalescence with a stationary interface, the tangential velocities along the drop surface and the interface, u_d and u_b, are zero. Only the second term on the right-hand side of (3.5) contributes to the pressure. As $(w_d$–$w_b)$ reduces quickly in the current experiments, the resulting lubrication pressure is not able to resist coalescence for a long time. Therefore, the drop coalesces rapidly with the bulk interface. When the interface is moving, the other two terms on the right-hand side come into effect and increase the lubrication pressure, thus delaying coalescence. The dynamics of lubrication flow and the resulting distribution of pressure for a drop resting on a moving interface will be analysed in detail in § 5.

4. General observations

4.1. *Drop deformation during initial impact with the interface*

After their release from the nozzle, the drops initially impact on the interface and rebound. Just before the impact, the velocity of the drop bottom starts to decrease while the upper part of the drop still accelerates due to gravity. By taking the drop bottom as a reference, the impact velocity is decreasing from approximately 4 cm s^{-1} in the vertical direction. As described in § 2, the impact velocity of the drops was kept the same by setting the nozzle at the same height and keeping the same flow rate of the drop phase for all tests. Figure 4(*a*) shows the changes in the drop and the interface shape during the impact and rebound period. The drop shape is characterized by the ratio of the horizontal to the vertical diameter, D_h/D_v. As can be seen, the changes in the drop shape are similar for all interface velocities. A typical case is presented in figure 4(*b*) for an interface of $v=3.4$ cm s^{-1}.

At the initial impact period between $t=0$ ms (when the drop starts to press against the interface) and approximately $t=30$ ms, there is large resistance to the downward

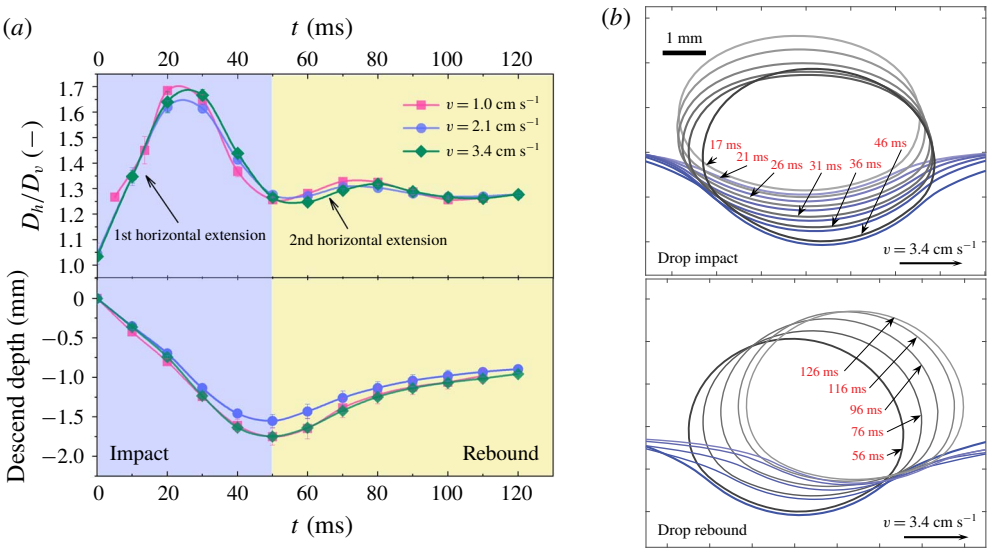

FIGURE 4. (*a*) Variation of the drop deformation characterized by the diameter ratio D_h/D_v and the descent depth of the drop bottom from its initial position at $t = 0$ ms when the drop contacts the interface; the data are averaged from five tests with standard deviation less than 6.8 %. (*b*) The impact and rebound of a single drop at the fluid interface of $v = 3.4$ cm s^{-1}.

movement to the bottom of the drop from the interface, while the top of the drop still moves downwards from the effect of gravity. As a result, the drop extends horizontally at approximately $t = 25$ ms to a maximum D_h/D_v of approximately 1.7. This is followed by the contraction of the drop and a reduction in D_h/D_v, driven by surface tension. The energy released from the drop contraction and the effect of gravity cause the drop to further descend until the interface reaches a minimum height at $t = 50$ ms. As is shown in figure 4(*b*), during the drop contraction from $t = 26$ ms to $t = 46$ ms, the height of the bottom surface of the drop decreases while the height of the upper surface of the drop slightly increases. The Laplace force from the deformed interface starts to push the drop upwards. This causes the drop to deform again and extend horizontally. However, the increase of the diameter ratio D_h/D_v and the drop deformation is far less than those in the impact period, as can also be seen from the drop shapes in figure 4(*b*).

The changes in the drop shape observed in the current experiments are similar to those reported by Mohamed-Kassim & Longmire (2003) for droplets impacting on stationary liquid–liquid interfaces. Two maxima of the horizontal diameter, similar to what is shown in figure 4(*a*), were observed as well in their tests. In addition, a minimum in the descending depth, at the end of the first horizontal extension of the drop, was also observed. As the impact velocity of the drops in the work by Mohamed-Kassim & Longmire (2003) (equal to the terminal velocity of the drop, which is 9.8–13.2 cm s^{-1}) is much larger than in the work here (<4 cm s^{-1}), the first maximum of the deformation of the drop D_h/D_v (1.72–2.28) is also higher than the one measured here.

A high impact velocity causes the drops to descend further into the interface. In the current experiments, the minimum descending depth of the droplet is approximately

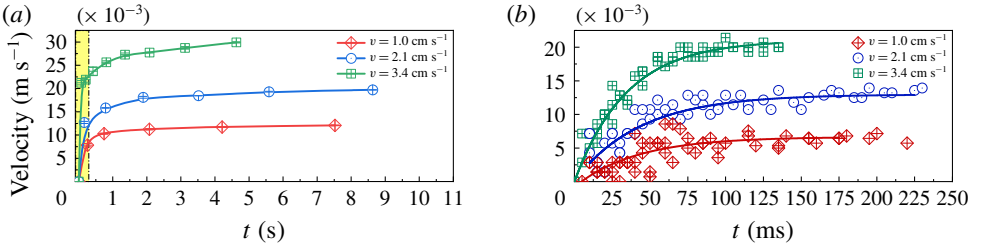

FIGURE 5. Change of drop velocity with time (*a*) over the whole measuring period, and (*b*) during the initial impact and rebound period. The velocity values in the legend are determined by tracking the motion of the drops at the final stage when the velocity is the same as that of the bulk interface. The fitting curves of the data are plotted in solid lines to help visualization.

$0.35D$ at $t = 50$ ms, where D is the volumetric equivalent diameter of the droplet. In the tests of Mohamed-Kassim & Longmire (2003), the descent depth could reach $1.1D$ at an impact velocity of 13.2 cm s^{-1}. A larger deformation of the bulk interface produces a stronger rebound of the droplet in the following stage. Accordingly, the maximum value of D_h/D_v in the second horizontal extension of the drop can even exceed the value of the first maximum under a large impact velocity of 13.2 cm s^{-1}. In the results shown here, the second maximum of D_h/D_v at the rebound stage is decreased to approximately 1.3. The oscillation time of impact and rebound varies a lot under different conditions. In the tests of Mohamed-Kassim & Longmire (2003), the second horizontal extension finished at 300–350 ms, while in this work the second maximum is reached much earlier at approximately $t = 100$ ms. The droplet oscillation is affected by many factors, including the impact height, the droplet size and the fluid properties (Hartland, Ramakrishnan & Hartley 1975; Mohamed-Kassim & Longmire 2003). Recently, Vakarelski *et al.* (2019) found that the mobility of the interface can also affect the drop rebound. In the current tests, the droplets are released from a height close to the interface to avoid large oscillations.

4.2. *Drop movement*

The velocity of a drop surfing along the moving interface is measured from the images by tracking the displacement of the central point of the maximum horizontal span of the drop. This is taken as a representative point for the velocity during the impact and the rebound stages, when the drop shape changes significantly and the velocities at different points of the drop can be different. For the period after the drop rebound, the shape of the droplet remains the same and any point in the drop can be used to track its velocity. As can be seen in figure 5(*a*), the drop speed increases fast initially during the impact and the rebound period (shaded area) for all interface velocity cases. This rapid increase is shown more clearly in figure 5(*b*). For the cases of low velocity ($v = 1.0$ cm s^{-1}), the drops reach almost the velocity of the interface at the end of this period. For the faster interfaces, the drop velocity continues to increase after the initial period but at a low rate until it reaches the velocity of the interface. The acceleration of the drops is believed to be caused by the drag force from the surrounding liquid both in the film region and in the outside area. A rough estimate, however, reveals that the drag force alone is not able to give this acceleration to the drop (see appendix A). Because of the uneven distribution of

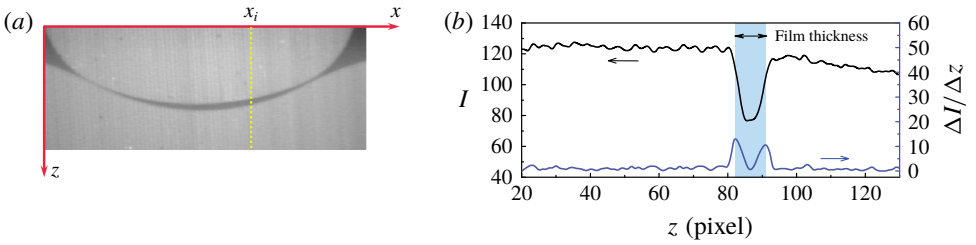

FIGURE 6. (*a*) Raw PLIF image showing the film shape. (*b*) Variation of the light intensity I (left axis) and intensity gradient $\Delta I/\Delta z$ (right axis) along the vertical dashed (yellow) line in panel (*a*).

the pressure in the film, the force acting normally on the drop bottom surface varies along the film. The integration of the local force along the drop surface is believed to produce a horizontal component that contributes to the drop acceleration along the flow direction.

4.3. *Film thickness*

The evolution of the film structure during the drop impact and rebound periods is discussed here. A typical PLIF image showing the shape of the film trapped between the drop and the oil–water interface is presented in figure 6(*a*). The fluorescent intensity along the vertical dotted line in the image is shown in figure 6(*b*). As can be seen, the light intensity is significantly reduced across the film region. The film thickness is calculated by measuring the vertical distance between the two z-points with maximum light gradient as proposed by Oldenziel *et al.* (2012).

For interface speed equal to $v = 1$ cm s^{-1}, a decrease of the film thickness along the flow direction is observed when the drop approaches the interface (see figure 7(*a*) from $t = 8$ ms to $t = 13$ ms). As the bulk interface at this time is not deformed significantly, the structure of the film is similar to the cases of a drop resting on a thin air film (Lhuissier *et al.* 2013; Sawaguchi *et al.* 2019). From $t = 13$ ms to $t = 23$ ms, the film thickness continues to decrease. At this stage, the film has a dimple shape with a thicker area at the centre and a thinner area at the border, which is commonly seen in the coalescence of drops with stationary interfaces (Klaseboer *et al.* 2000). According to (3.5), while the drop is approaching the interface, the tangential velocity of the interface is low, and the velocity difference $(w_d - w_b)$ is the dominant term in the calculation of the film lubrication pressure. It has been shown that the lubrication pressure resulting from a drop approaching a flat interface has an approximately concave shape with a peak near the centre (Yiantsios & Davis 1990). The film, therefore, thins more slowly at the centre than at the border and acquires a dimpled shape.

During the drop rebound period, after $t = 58$ ms, the film thickness should continue to decrease as the liquid in the film is still draining. However, the central part of the film seems to refill and form a peak from $t = 58$ ms to $t = 83$ ms, as shown in figure 7(*b*). It is believed that it is not only the uneven distribution of the pressure in the film that causes the formation of the peak but also the horizontal shrinkage of the film. Figure 8(*a*) illustrates the change of the horizontal locations of the minimum film thickness points over time. The distance between the two points, regarded as the film width, is shown in figure 8(*b*). For interface speed of $v = 1.0$ cm s^{-1}, the film

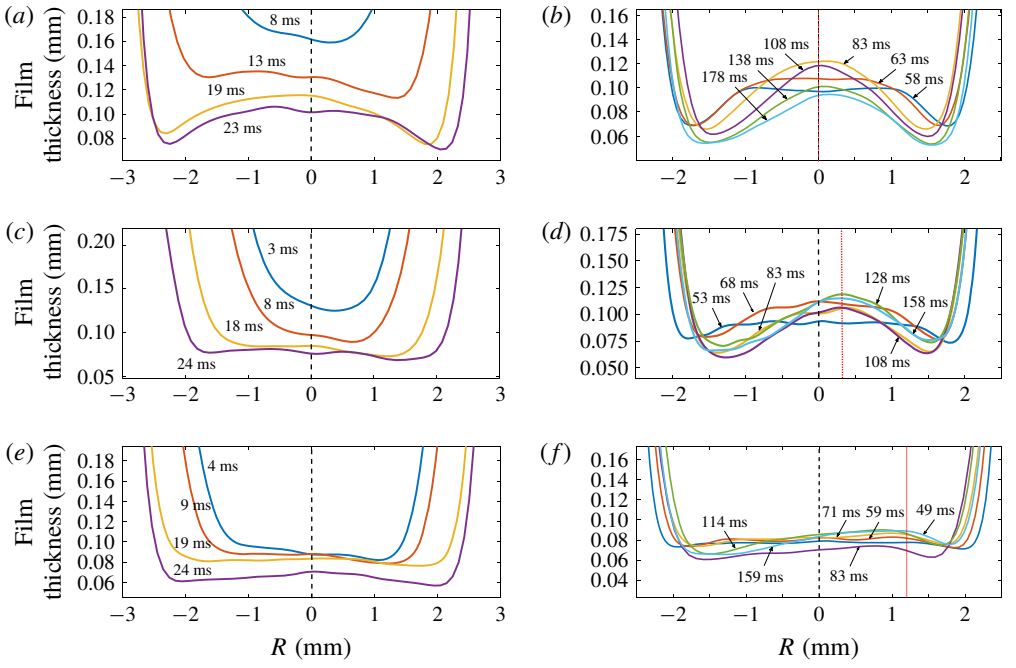

FIGURE 7. The variation of the film thickness during drop impact and rebound at bulk interface velocities (*a*,*b*) $v = 1.0$ cm s^{-1}, (*c*,*d*) $v = 2.1$ cm s^{-1}, and (*e*,*f*) $v = 3.4$ cm s^{-1}. The vertical dotted (red) lines represent the locations with the maximum film thicknesses at the last time step of the measurement.

has expanded to a maximum width at approximately $t = 30$ ms, after which the width starts to decrease until a minimum value is reached at $t = 100$ ms. This horizontal film contraction is believed to accumulate the liquid in the centre and to generate the peak. As the width of the film slightly increases after 100 ms (figure 8*b*), the refill of the film stops and the film continues to thin while preserving its dimpled shape. The effect of the interface speed is low for this case, and the peak of the film thickness is located at the centre.

For the higher interface speed of $v = 2.1$ cm s^{-1}, the tangential velocity along the interface also contributes to the lubrication pressure in addition to the drop approaching velocity. As will be discussed in § 5, the pressure tends to be uniformly distributed in the film in this case and the dimpled structure is not as obvious as for $v = 1$ cm s^{-1}, as shown in figure 7(*c*) during the drop impact from $t = 3$ ms to $t = 24$ ms. During the drop rebound, the film also refills and a peak is formed. At $t = 53$ ms, the film forms a plateau around the centreline. Between $t = 53$ ms and $t = 100$ ms (figure 8*a*), the thin part of the film upstream moves faster than that one downstream. As a result, the film peak is slightly shifted downstream. When the interface speed increases to $v = 3.4$ cm s^{-1}, the interface velocity contribution to the lubrication pressure is further increased and the dimple structure is less obvious. During the rebound, the film width does not contract as much as in the lower interface velocities (figure 7*d*) and the refill is not obvious. In addition, the peak is shifted further away from the centre compared to $v = 2.1$ cm s^{-1}.

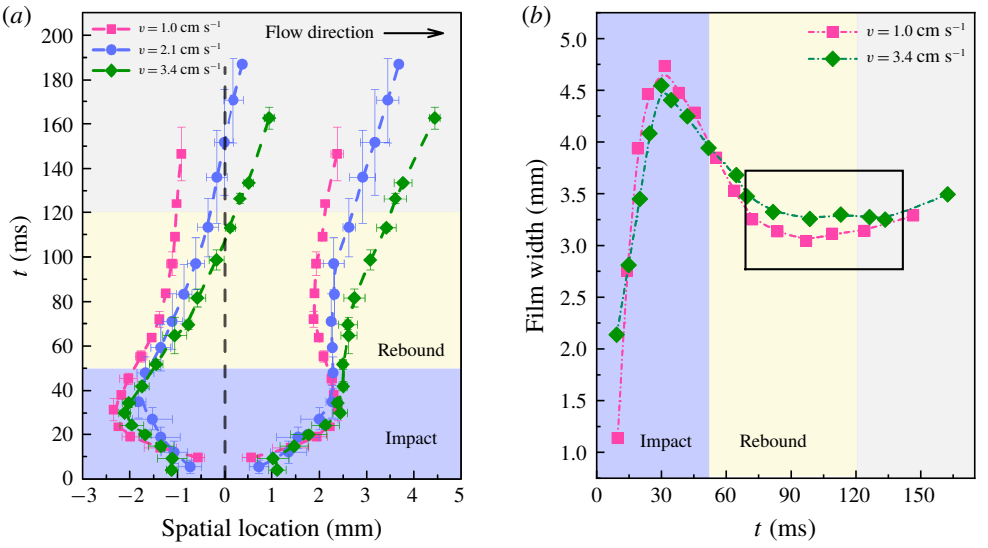

FIGURE 8. (*a*) Variation of the horizontal locations of the minimum film thickness against time t. The initial values were taken at 5 ms after the drop contacts the bulk interface. (*b*) Evolution of the film width; only the cases $v = 1.0$ cm s^{-1} and $v = 3.4$ cm s^{-1} are shown to help visualization.

4.4. *Drop inner circulation*

The velocity of the liquid inside the drop was measured with PIV. This is shown for a moving interface of $v = 2.1$ cm s^{-1} in figure 9. To observe the circulation patterns and isolate the circulation from the horizontal motion of the drop, the horizontal translational speed of the centre of mass of the drop was subtracted from the local velocity. During the initial impact and rebound period, no circulation is seen as the drop undergoes a large deformation. Shortly after, recirculation appears in the drop, as shown in figure 9(*a*). At this time, the drop rotates like a rigid body with the centre of rotation coinciding with the drop centre, which is similar to what was previously observed for drops resting at a hydraulic film jump (Sreenivas *et al.* 1999) and on a steady air film (Sawaguchi *et al.* 2019). But unlike those cases, as the drop accelerates to the velocity of the interface, the inner circulation decays.

When the drop travels to $L = 0.5$ cm away from the impact point, the velocity at the lower part of the drop becomes comparable to that in the bulk. The shear force acting on the bottom surface of the drop is believed to decrease. On the other hand, the average speed of the drop becomes higher than that of the surrounding oil phase. The shear force on the upper surface of the drop from the surrounding oil contributes to the circulation inside the drop and a backflow with large velocity in the top area of the drop is observed. This is not balanced by the shear force at the bottom of the drop and the centre of rotation does not coincide with the drop centre any more. At $L = 1$ cm, the centre of rotation covers a wide area close to the bottom of the drop, which indicates that the shear force at the bottom surface is small. At $L = 2$ cm, only the liquid in the upper part of the drop has a backward flow, while the rest of the drop liquid travels with the same velocity as the average drop speed. The backward flow seen in figures 9(*c*) and 9(*d*) at the top of the drop is not balanced by an equivalent forward flow near the bottom of the drop and suggests that there

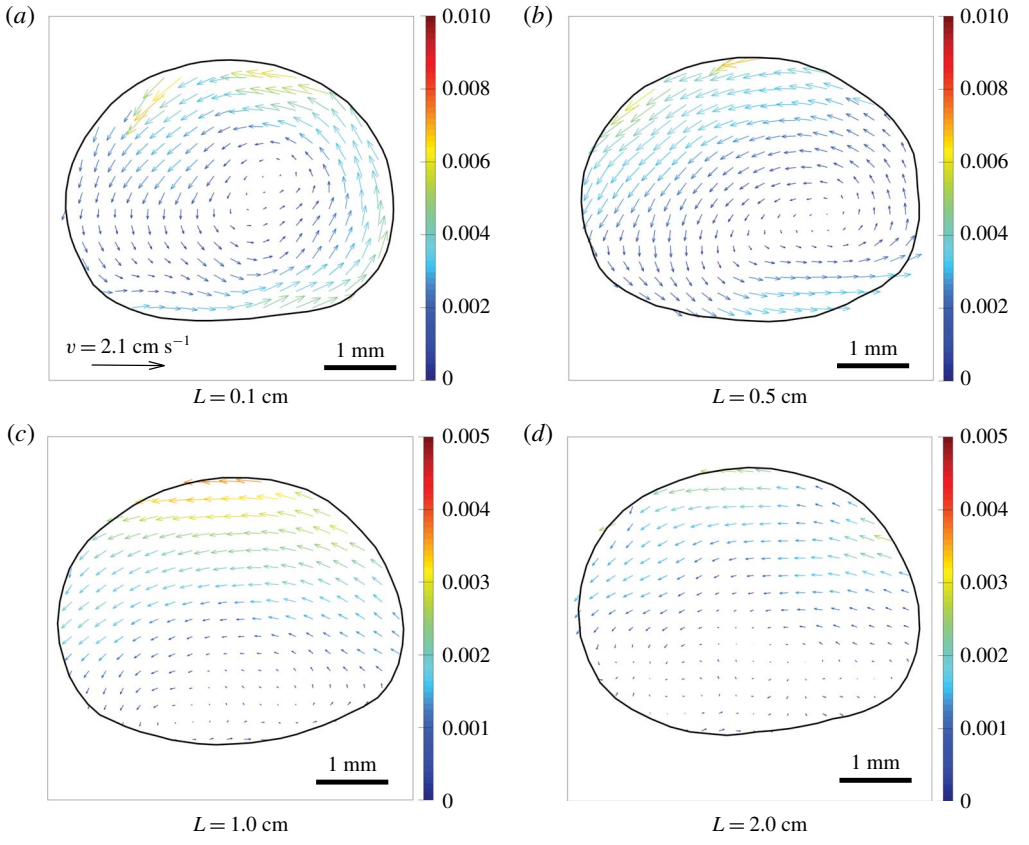

FIGURE 9. Velocity fields (m s^{-1}) in the drop at different locations away from the impact point for $v = 2.1$ cm s^{-1}. The velocity is the value relative to the translational velocity of the drop, which is measured by detecting the trajectory of the centre point of the drop. The solid lines outline the drop surface.

is no mass conservation of the liquid in the drop. Both Sreenivas *et al.* (1999) and Sawaguchi *et al.* (2019) commented that the internal flow in a drop levitated on a moving surface is complicated. Some of their results have shown that secondary flows appear at the bottom of the drop with direction out of the measuring plane. To analyse these phenomena qualitatively, three-dimensional velocity profiles would be needed.

5. Lubrication flow in the film

5.1. *Lubrication flow*

As discussed above, the lubrication pressure in the film is considered to be responsible for the delayed coalescence of the drop with the interface. However, the film thickness is not uniform, while both the drop surface and the oil–water interface are moving, which would make simulations challenging. Instead, a simplified approach was followed here to explore the lubrication pressure variation in the film. It was found that a drop, pendent from the nozzle, did not coalesce with a moving interface for a very long time (see Movie 2 and figure 10*a*). In a similar case reported by Dell'Aversana *et al.* (1996), of a drop contacting a moving liquid surface, a wake was

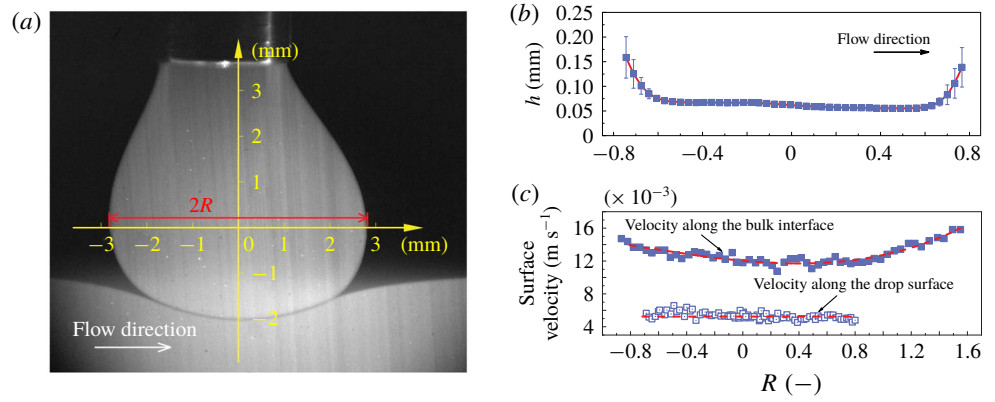

FIGURE 10. (*a*) A pendent drop resting on the interface without coalescence. The origin of the axes is at the centre of the maximum width of the deformed drop, which is defined as $2R$. (*b*) Thickness of the film trapped between the drop surface and the liquid–liquid interface. The film thickness is averaged from five different times when a drop levitates on the interface, and the error bars show the standard deviation. (*c*) The magnitude of the velocity along both the drop surface and the interface of the bulk liquid. The spatial location is normalized by the drop 'radius' R.

observed on the interface after the drop has passed. In the current system, no wake was seen, perhaps because the thickness of the bulk liquid is large, approximately 15 cm, and there is no effect from the bottom wall on the interface flow as was seen by Dell'Aversana *et al.* (1996).

The thicknesses of the film trapped between the drop and the bulk homophase at various time steps was measured. As shown in figure 10(*b*), the film thickness slightly decreases along the flow direction while the film structure does not change significantly with time. Therefore, the case can be regarded as a steady-state process. To investigate the lubrication pressure in the film, a numerical simulation is set where the drop surface and the bulk interface are regarded as solid boundaries with a given tangential velocity. These velocities are taken from the experimental data. The velocity at the bulk interface is found to decrease along the flow direction until a minimum value is reached roughly at the centre point. Afterwards, the velocity increases further downstream. The velocity along the drop bottom surface is almost constant in the region of the thin film (see figure 10*c*). The velocities along the bulk interface and the drop surface are measured by tracking the motion of the particles in the vicinity of the interface. The methods and the details of the simulation are discussed in appendix B.

Figure 11(*a*) shows the simulated pressure in the trapped film. As can be seen, the pressure is positive in the majority of the film region. This pressure resists the contact of the drop surface with the oil–water interface. In the current experiments, as the drop approaches, the oil–water interface deforms more than in the cases reported in the literature of drops levitated over a thin layer of air (Sawaguchi *et al.* 2019). As a result, the pressure distribution calculated here is slightly different from the former cases. In the experiments of Sawaguchi *et al.* (2019), the pressure in the film region is almost constant except for a sharp decrease at both the entrance and the exit sides of the film. In the current work, the pressure increases along the flow direction from the film entrance to the centre, where a peak is observed. Downstream from the centre,

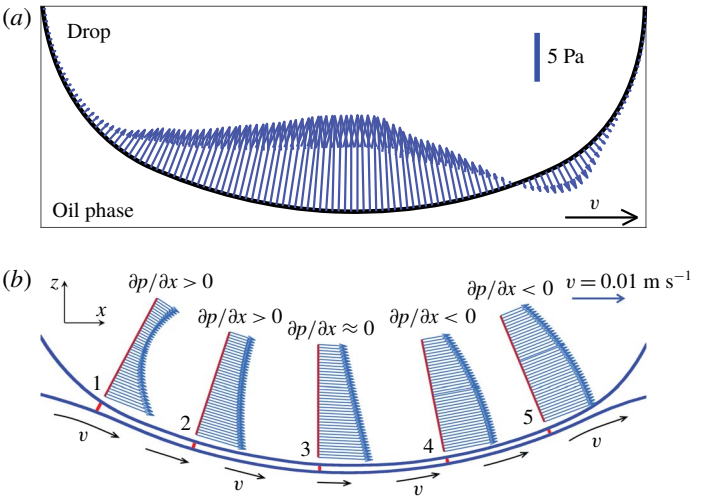

FIGURE 11. (*a*) The lubrication pressure along the film. (*b*) Velocity profiles at different locations in the trapped film for the case of a pendent drop on the moving interface as shown in figure 10(*a*).

the pressure decreases until a minimum value is reached at the exit of the film. As discussed by Sawaguchi *et al.* (2019), the negative pressure in the film, which tends to pull the interfaces together, is balanced by the Laplace force created by the local surface deformation. Thus coalescence is effectively prevented. Once the drop surface curvature is not able to balance the low pressure, the film breaks and coalescence is observed in the corresponding location. A typical case of such coalescence is shown in Movie 3.

The variation of the lubrication pressure in the trapped film also affects the velocity profile. As shown in figure 11(*b*), the liquid near the film entrance roughly at location 1 is pulled in to the film by the bulk moving phase. From the film entrance at location 1 along to the approximately central position at location 3, the velocity has a concave shape along the cross-section of the film. Downstream of the central point, the drop motion pushes the film liquid out, and the velocity profile acquires a convex shape. The variation of the velocity profile in the film agrees well with the profiles in lubrication oil films in classical lubrication theory (Hamrock *et al.* 2004).

5.2. *Lubrication pressure*

At any point on the drop surface, the internal pressure in the drop is balanced by the external pressure in the film and the Laplace pressure resulting from the interface curvature:

$$P_{in} = P_{out} + \sigma(\kappa_r + \kappa_z), \tag{5.1}$$

where P_{in} and P_{out} refer to the pressure inside the drop and in the film, respectively. The pressures P_{in} and P_{out} combine both the hydrostatic pressure due to the density difference between the droplet and the surrounding liquid and the hydrodynamic frictional pressure. In (5.1), κ_r is the main curvature of the surface and κ_z is the curvature normal to κ_r. Applying (5.1) in the film flow, the lubrication pressure can be estimated if the local curvature of the drop surface and the drop internal pressure

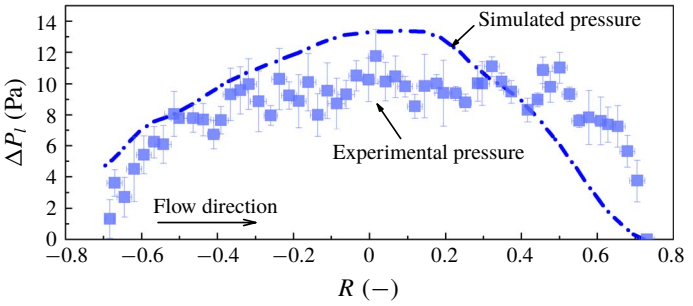

FIGURE 12. Comparison of the film pressure calculated by the local curvature of the pendent drop surface with the numerically simulated pressure. The data shown are averaged from the pressures at five different time steps. The error bars show the standard deviation.

are known. For an accurate estimation of the pressure, the two components of the curvature κ_r and κ_z should be known. However, in the current experiments, where only the two-dimensional profile of the drop is acquired, the azimuthal component of the curvature is unknown. As the drop bottom in the film region is relatively flat under the pressure from the bulk interface, the azimuthal component of the curvature is considered small and is neglected (Duchemin, Lister & Lange 2005; Lhuissier *et al.* 2013). The pressure variation was estimated with the PIV velocity data according to the methods explained by Oudheusden (2013). Inside the drop it was found that the pressure variation induced by the internal flow is much lower than the hydrostatic pressure. Thus, only the hydrostatic pressure is considered. The lubrication pressure in the film relative to the pressure at the film exit p_0, where the drop surface curvature is maximum, is calculated as follows:

$$\Delta P_l = (\rho_d - \rho_s)gH + \sigma(\kappa_0 - \kappa_i), \tag{5.2}$$

where κ_0 and κ_i are the curvature at the reference point p_0 at the film exit and at a point p_i in the film region considered.

The variation of the pressure for the case discussed in § 5.1 (see figure 11) is shown in figure 12. It is seen that the pressure values calculated from (5.2) are slightly lower than the simulated ones in most of the film region. As previously discussed by Smith & Neitzel (2006) and Lhuissier *et al.* (2013), flow can also occur in the film in a direction lateral to the main flow in the experiments. In the two-dimensional simulations, however, there is no lateral flow and all the liquid entering the film flows in one direction and contributes to the lubrication pressure. The pressure values calculated from (5.2) are higher than the simulated ones in the area near the film exit. A similar discrepancy was also observed by Lhuissier *et al.* (2013), who, based on a similar approach, found that the calculated air film shape differs a lot from the measured shape in the region near the film exit. The error is attributed to the effects of the azimuthal component of the curvature, which is not taken into account in the calculation.

Equation (5.2) is then used to calculate the lubrication pressure in the film in the different cases studied. As the shape of the film evolves over time, the corresponding lubrication pressure changes as well. For all the interface speeds studied, the lubrication pressure is calculated when the drop recovers to a steady shape and

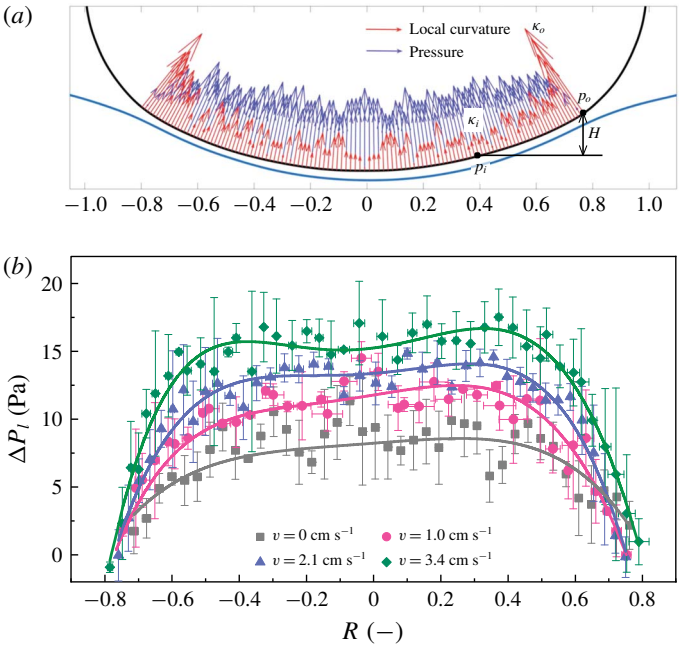

FIGURE 13. (*a*) Relative lubrication pressure ΔP_l at any point p_i in the film for the case of a moving drop on the interface with velocity $v = 3.4$ cm s^{-1} after the rebound. The pressure at point p_0 at the film exit is taken as reference. (*b*) Magnitude of ΔP_l in the film between the travelling drop and the bulk interface at different velocities and at t = 130 ms. The pressure value is averaged over five different tests and the error bars show the standard deviation.

constant speed at t = 130 ms after the drop impacts the interface (see figures 4 and 5). Figure 13(*a*) illustrates the variation of the surface curvature at the bottom of the drop, as well as the corresponding pressure distribution at $v = 3.4$ cm s^{-1}, as an example. The relative pressure in the film at different interface speeds is shown in figure 13(*b*).

As can be seen, when the drop is settled on the interface after the rebound, there is a large lubrication pressure in the film region, which resists the coalescence of the drop with the bulk interface. Consistently with what is predicted by (3.5), the pressure magnitude increases with the interface speed. The pressures shown in figure 13(*b*) are positive throughout the film region, because their magnitudes are relative to a minimum pressure at the film exit. When the absolute pressures are considered, then negative values are found at the film exit for all the cases investigated, similar to what is shown in figure 11(*a*). As discussed in § 5.1, once the negative pressure exceeds the magnitude that the Laplace pressure is able to resist, the two interfaces will be pushed together, resulting in film rupture (Sawaguchi *et al.* 2019).

6. Drop coalescence

Coalescence occurs when the film separating the drop from the interface thins sufficiently for the van der Waals forces to become significant and cause its rupture (Hahn, Chen & Slattery 1985). At the location of the film rupture, the liquid in the drop moves rapidly and helps locate the rupture point on the drop surface with

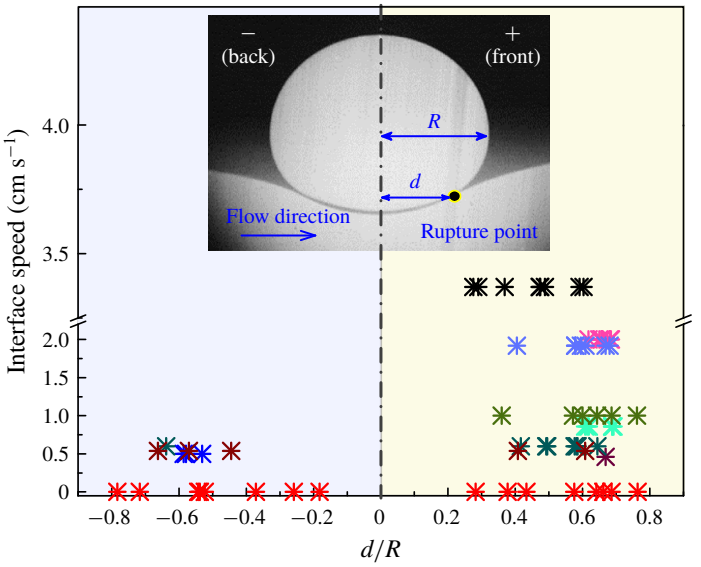

FIGURE 14. Distribution of rupture points for an interface with different speeds. The data acquired from different coalescence events are marked by different colours.

high-speed imaging. Figure 14 shows the rupture points for all the coalescence events observed in the experiments. For the stationary interface, the rupture points are distributed equally around the drop middle point. Rupture rarely occurs near the centre, which is in good agreement with previous findings that the rupture points occur near the rim where the film is thinnest (Mohamed-Kassim & Longmire 2004; Oldenziel *et al.* 2012). At an interface speed of $v = 0.5$ cm s^{-1}, more of the rupture points are in the front of the drop centre than at the back. Interestingly, most of the rupture events at the back are observed shortly after the impact due to instabilities. In contrast, the rupture events at the front usually occur after the drops have travelled some distance ($L > 5$ cm). At higher interface speeds, all rupture points are located at the front part of the film. It has been shown that, when a drop travels along a stationary interface (Hale & Akers 2016), the rupture points also tend to appear on the front part of the drop, in the direction of the flow, rather than at the back.

It is suggested that the locations of the rupture points are closely related to the spatial distribution of the lubrication pressure in the trapped film. For most of the cases where drops levitate on a moving liquid surface, the trapped air film thickness monotonically decreases from the upstream to the downstream location (Sreenivas *et al.* 1999; Lhuissier *et al.* 2013; Davanlou 2016; Sawaguchi *et al.* 2019). According to the classical lubrication theory, the generated pressure in the air film is able to make the drops levitate. As was shown in § 4.2, the variation of the film shape for drops approaching a liquid–liquid interface is more complex than in the case of drops approaching an air–liquid surface. After the drop rebound, the film still has a dimpled shape. The film thickness continues to evolve as the drop is travelling along the interface, as shown in figure 15 for two different locations. As the film thickness is close to the spatial resolution of the high-speed camera at distances larger than $L = 2$ cm, only film thicknesses for shorter distances are measured. As can be seen, between the drop rebound location (as shown in figure 7) and a distance $L = 1$ cm, the film thickness decreases significantly in the upstream part of the drop and is

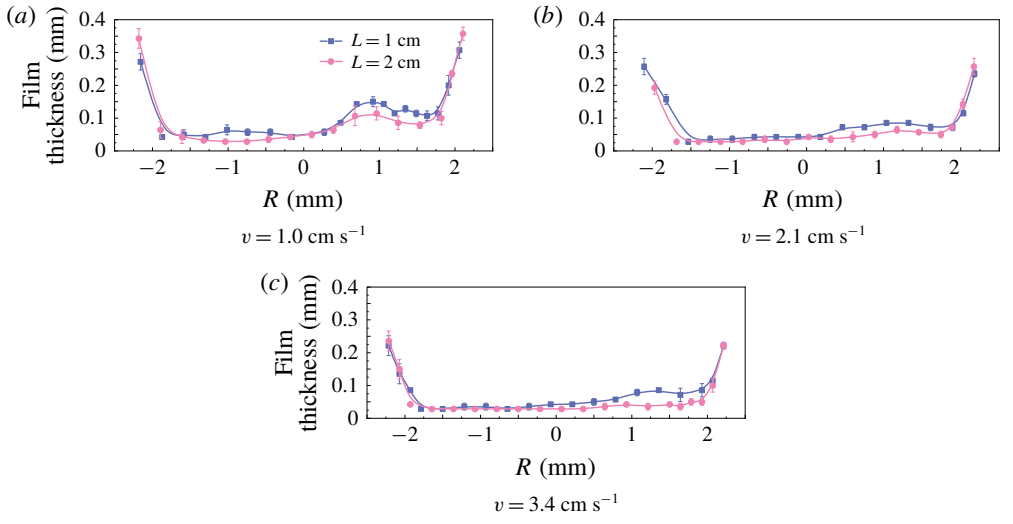

FIGURE 15. Film thickness at two different locations L from the drop impact point for interfaces of different speeds.

almost uniform (left half of the film shown in figure 15) for all interface speeds. At the downstream part of the drop, the dimple structure survives and the film is thicker. The thinning of the film in the upstream location increases locally the lubrication pressure (Sreenivas *et al.* 1999), which prevents the drop from further approaching the interface. As a result, the rupture is less likely to happen in the upstream part of the drop, even though the film is thinner there than in the downstream location.

When the drops travel further downstream, the film thickness at the upstream part does not change a lot while it decreases at the front but still remains larger than at the back. As discussed previously, the expansion of the film in the dimple results in a low lubrication pressure in the corresponding area. The low pressure in this region is considered to be responsible for the rupture points to occur in the front part of the film, as shown in figure 14.

7. Oil entrainment

When a drop coalesces with a stationary interface, a meniscus is created immediately after the film rupture, which expands rapidly until the liquid in the drop completely merges with the bulk homophase. The expansion of the meniscus is resisted by the viscosity of the fluids at the initial stages, and later by the inertia of the liquids (Aarts & Lekkerkerker 2008; Murano & Okumura 2018; Dong *et al.* 2019). It was found, however, that when drops coalesce with moving interfaces, the trapped film, before it fully drains, can break into 'drop-strings', where different-sized drops form connected with thin threads. The breakage of the film into drops observed here is different from what was found previously for a drop coalescing with a moving air–liquid interface. In the experiments of Hale & Akers (2016), the air film breaks into scattered bubbles, resulting in a Mesler entrainment (Esmailizadeh & Mesler 1986). However, in the current experiments, the satellite drops produced by the breakage of the film remain connected to each other with oil-phase threads.

The breakage of the trapped film and the spatial evolution of the drop-string in the case of a drop coalescing with interfaces moving at $v = 2.1$ cm s^{-1} and

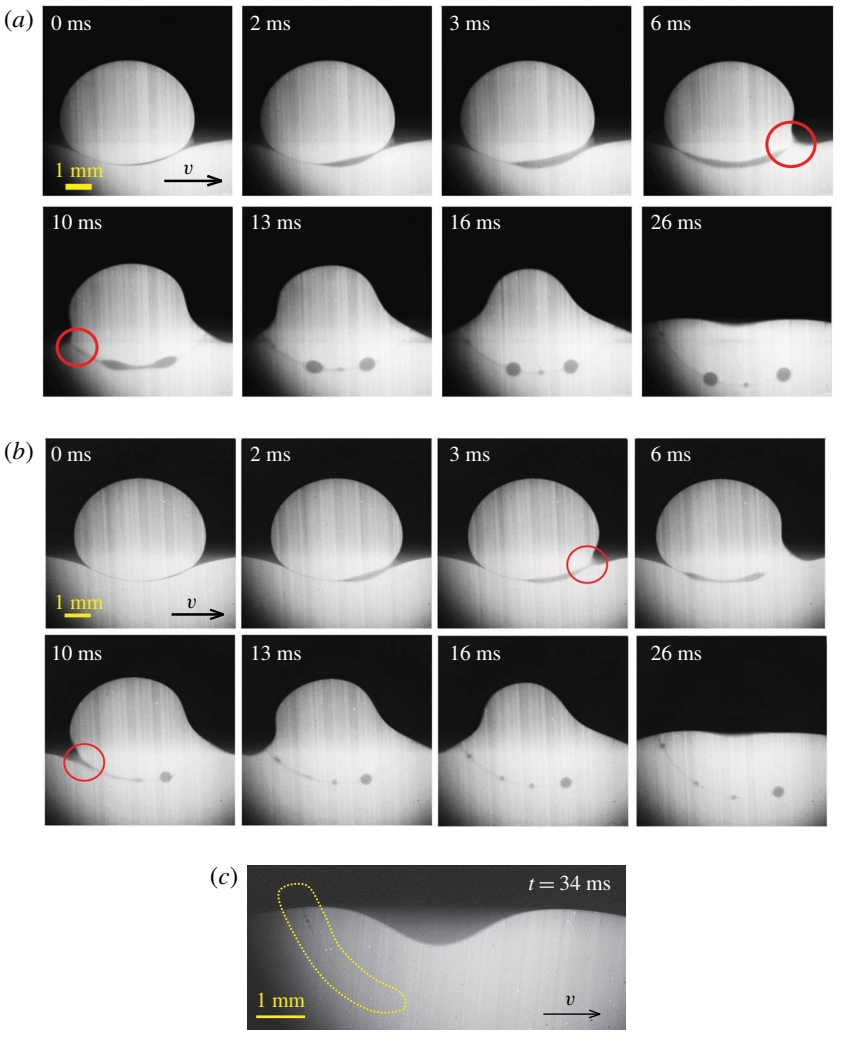

FIGURE 16. Formation of the 'drops on a string' during the coalescence of drops with moving interfaces with speeds of (*a*) $v = 2.1$ cm s^{-1}, $L = 0.5$ cm and (*b*) $v = 3.4$ cm s^{-1}, $L = 1$ cm. (*c*) Incomplete drop-string formation for a coalescence event at $v = 3.4$ cm s^{-1}, $L = 5$ cm.

$v = 3.4$ cm s^{-1} is presented in figure 16. The coalescence of the drop at the interface of $v = 3.4$ cm s^{-1} is shown in Movie 4 as a representative. The drop-strings shown in figure 16(*a*,*b*) are obtained with relatively thicker films. If the trapped film is thin at the moment of rupture, the resulting drop-string is not fully linked with the left and right interfaces. Instead, only a tendril linking the drop to the oil phase is observed (see the area circled by a yellow line in figure 16(*c*)), which is similar to what was shown previously (Aryafar & Kavehpour 2008; Oldenziel *et al.* 2012). The drop-strings produced here are similar to the breakage of a viscoelastic filament (Bhat *et al.* 2010). As the drop-strings were not seen to form in the case of a drop coalescing with a stationary interface with the same liquids, it is believed that the

phenomenon is not caused by contamination that may change the interfacial properties of the fluids.

When a drop coalesces with a stationary interface, the meniscus that forms after rupture increases and the film can drain from all sides of the drop until it is completely drained. However, when the coalescence is with a moving interface, it was found that, before the film can completely drain, another coalescence event appears at the side of the drop leading to oil entrained in the bulk water phase, as shown by the areas circled in red in figure 16(*a*,*b*). Subsequently, the entrained oil film starts to form drops under the influence of interfacial tension resulting in the 'drops on a string' structure. The capillary waves, initially created at the onset of the film rupture, may further hinder the trapped oil to contract to a liquid body and favour the generation of the drop-strings (Charles & Mason 1960).

8. Conclusions

Surfing of drops and delayed coalescence on moving liquid–liquid interfaces is relevant to many industrial applications but has not been studied previously. The aim of this work is to explore the behaviour of travelling aqueous drops on moving oil–water interfaces. Studies were carried out in a novel flow channel, using a combination of PLIF and PIV techniques to obtain the evolution of the shapes of the drops, of the film thickness and of the tangential velocities at the drop surface and the bulk liquid–liquid interface, as the drops impact on the interface and move along. It was found that drop coalescence is delayed by the moving interface and that the delay increases with the interface speed. The delay is attributed to the lubrication pressure in the film trapped between the drop and the interface. This pressure was calculated based on the local curvature of the drop surface and the tangential velocities on the drop surface and on the bulk interface in the film region. For the case of a stationary drop, the results were also compared with numerical simulations with good agreement. The results reveal that the lubrication pressure is high along most of the film, preventing the drop from approaching the interface, and increases with the interface velocity. The film has a dimple shape, with increased thickness close to the exits, which locally decrease the lubrication pressure. The reduced pressure in the dimple regions allows the drop to approach the interface and will eventually lead to film rupture. As the interface velocity increases, the dimple shape becomes less obvious, especially at the upstream part of the drop. As a result, with increasing interface velocity, film rupture occurs at the downstream part of the drop, where the film retains its dimple shape.

The current findings will be relevant to studies of dispersed flows and their separation (Rommel *et al.* 1993), in drop manipulation in microfluidic systems (Deng *et al.* 2016) and in printing applications (Fathi, Dickens & Fouchal 2010). Further work is needed to understand the delayed coalescence. Previous studies by Sawaguchi *et al.* (2019) have shown that the circulation inside the drop is complex and three-dimensional, while the results shown here only describe the circulation in the laser plane. The flow and characteristics of the film were also only observed in a two-dimensional plane. Volumetric PIV approaches will elucidate the flows in the drop and in the film. In addition, it is still unclear how the film breaks into the 'drops on a string' configuration, and this merits further studies.

Acknowledgements

This project was funded by the UK Engineering and Physical Sciences Research Council (EPSRC) Programme Grant MEMPHIS. T.D. would also like to thank the Chinese Scholarship Council (CSC) for providing his studentship.

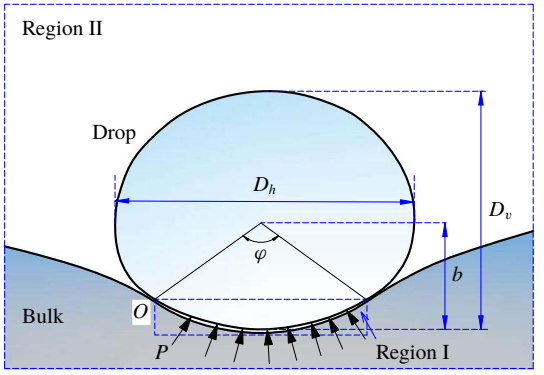

FIGURE 17. Geometric variables of drop on a deformed interface.

Declaration of interests

The authors report no conflict of interest.

Supplementary movies

Supplementary movies are available at https://doi.org/10.1017/jfm.2020.192.

Appendix A

The acceleration of the drop is attributed to the drag force from the surrounding liquid and the force from the interface on the bottom of the drop. As shown in figure 17, in the 'inner' region I, where the drop bottom is very close to the interface, the flow pattern is different from that in the 'external' region II. The drag forces on the drop surface will also be different in these two regions. The drag force on a sphere that is fully submerged in oil with a relative speed Δv is estimated by Nakayama (2018) as

$$F_{oil} = C_d \frac{\pi D_v^2 \rho_{oil} (\Delta v)^2}{8}, \tag{A 1}$$

where C_d is the drag coefficient, D_v is the vertical diameter of the drop and Δv is the velocity of the oil phase relative to the drop. From the numerical simulations (discussed in appendix B), the average velocity of the oil phase surrounding the drop was found to be approximately half of the interface velocity. The corresponding Reynolds number $Re = \rho D \Delta v / \mu$ is almost 50 at the beginning of the impact period when the velocity difference between the drop and the interface is large. When the drops reach the speed of the surrounding liquids, Re is reduced to approximately 0.02. According to Dijkhuizen *et al.* (2010), the drag coefficient C_d for drops can be calculated from (A 2), which is valid both in the Stokes region as well as at higher Re:

$$C_d = \frac{16}{Re}\left(1 + \frac{2}{1 + \dfrac{16}{Re} + \dfrac{3.315}{\sqrt{Re}}}\right). \tag{A 2}$$

Since only part of the drop is affected by the surrounding oil phase in the 'external' region II, a correction factor $\beta = \frac{2}{5}(2 + (D_v - b/D_h))$, which depends on the drop

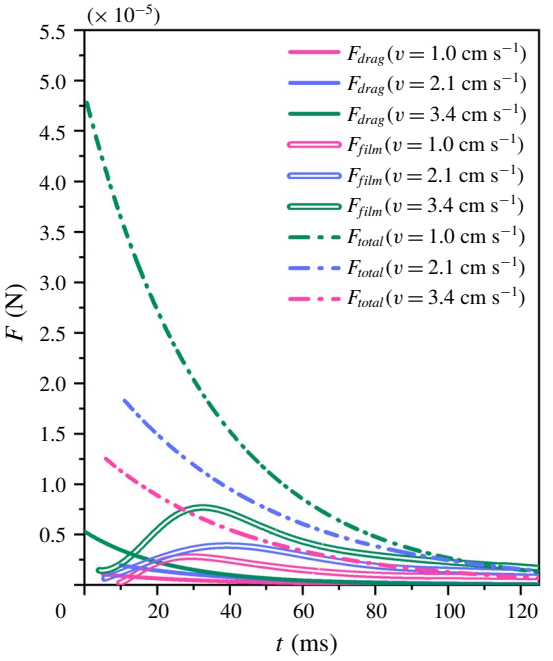

FIGURE 18. Variation of the total force F_{total} that the drops require for the acceleration, the estimated drag force F_{drag} from the surrounding liquids and the tangential force F_{film} from the film at the bottom of the drop.

geometry, needs to be introduced to take this into account (Hale & Akers 2016). As shown in figure 17, b is the minor axis of the bottom of the drop.

In the 'inner region' I, the shear force on the drop bottom surface is expressed as $\tau = \mu(\partial u/\partial h)$, where h is the film thickness, which is approximately 0.1 mm at the impact period. According to Sreenivas *et al.* (1999), a linear variation of the velocity is considered across the film region. The tangential velocity along the bulk interface, u_b, is considered equal to the final velocity of the drop, which is found from figure 5. The velocity along the drop bottom surface is taken equal to zero, because no inner circulation in the drop was observed at this stage. The tangential shear force is thus estimated by integrating the shear stress along the bottom surface in region I.

The variations of the total force F_{total} required to accelerate the drop (which is calculated based on figure 5), the drag force from the surrounding liquid, F_{drag}, in region II and the shear force in the thin film, F_{film}, in region I at the initial stages are shown in figure 18. As can be seen, the shear force F_{film} from the film in the inner region I contributes more than the drag force F_{drag} from the surrounding oil most of the time. At the beginning ($t < 15$ ms), the relative velocity between the drop and the surrounding liquid is large, while the film area is small and the drag force F_{drag} is comparable to F_{film}. Afterwards, the drag force, F_{drag}, decreases as the relative velocity between the drop and the surrounding liquid diminishes rapidly, while the shear force, F_{film}, in the film is increasing as its length increases. After a transition point, the shear force F_{film} decreases as the film region starts to shrink. Figure 18 reveals that the combined F_{drag} and F_{film} forces are less than the force required to accelerate the drop, especially at the initial stages of drop rest, before $t = 30$ ms. It is believed that the Laplace force due to the deformation of the interface and the uneven

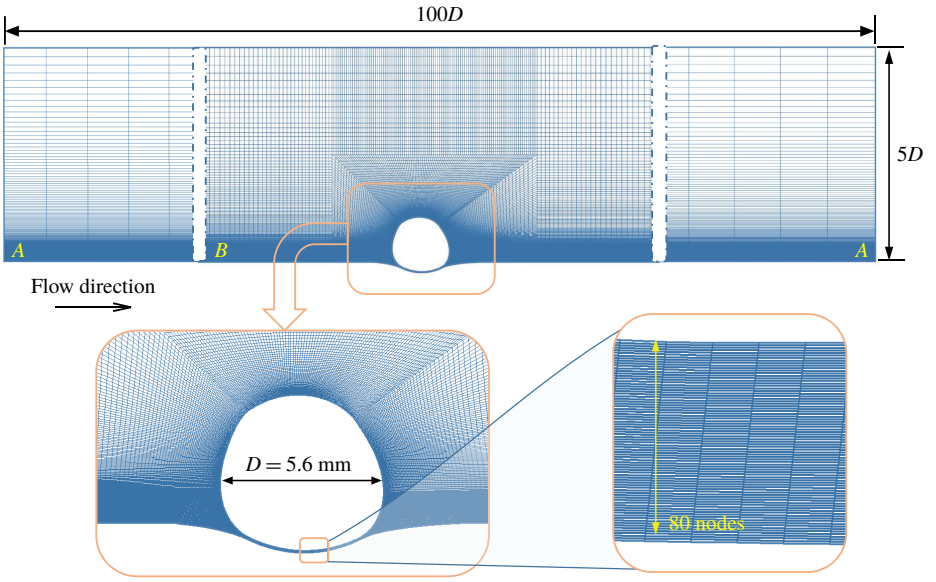

FIGURE 19. Computational domain and details of the grid used around the drop and in the film region (total number of cells 1 28 053).

distribution of the flow-induced lubrication pressure in the trapped oil film generate a horizontal force that also contributes to the acceleration of the drop.

Appendix B. Estimation of the pressure (Pa) in the trapped film through simulation

The flow in the thin film trapped between the stationary drop and the bulk interface in § 5.1 is simulated with ANSYS Fluent 19.2. As described in § 5.1, the drop shape and the film thickness do not change during the whole process, which is regarded as steady state. The Reynolds number $Re = \rho uh/\mu$ in the thin trapped film is much lower than 1 (Sawaguchi *et al.* 2019) and the lubrication theory can be applied. However, to get more accurate results, the inertial term is not ignored and in the simulation the full Navier–Stokes equations are considered. A two-dimensional simulation is carried out, where the steady-state shape of the drop and of the local film thickness are extracted from the experimental measurements by tracking the motion of the particles that are near the drop surface and the bulk interface. In the simulations it is assumed that the whole drop is surrounded by the oil phase and the nozzle is omitted. This is justified because at the level of the nozzle the oil velocity is close to zero and the effect of the nozzle on the flow field in the film region is expected to be negligible. As shown in figure 19, the drop is located at $50D$ away from both the inlet and the outlet to avoid end effects. A relatively coarse mesh was set in region A near the inlet and the outlet. A refined mesh was used in the drop region B, with a smooth transition to region A. The mesh in the film, whose thickness is approximately 50 μm, is further refined to 80 nodes across the film height to improve the simulation accuracy. In the simulations, both the drop surface and the bulk interface are considered as solid walls with tangential velocities equal to those measured experimentally, as shown in figure 10(*c*). For the interface, a velocity of 2 cm s^{-1} was used. The calculations were

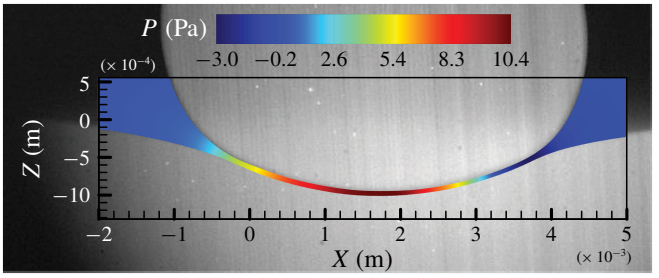

FIGURE 20. Contour of the pressure field in the trapped film and in the surrounding area.

carried out at atmospheric pressure and the simulated pressure distribution in the film is shown in figure 20.

REFERENCES

AARTS, D. G. L. & LEKKERKERKER, H. N. W. 2008 Droplet coalescence: drainage, film rupture and neck growth in ultralow interfacial tension systems. *J. Fluid Mech.* **606**, 275–294.

ANDRADE, B., SONG, Z. Y., LI, J., ZIMMERMAN, S. C., CHENG, J. J., MOORE, J. S., HARRIS, K. & KATZ, J. S. 2015 New frontiers for encapsulation in the chemical industry. *ACS Appl. Mater. Interfaces* **7** (12), 6359–6368.

ARYAFAR, H. & KAVEHPOUR, H. P. 2008 Hydrodynamic instabilities of viscous coalescing droplets. *Phys. Rev.* E **78** (3), 037302.

BHAT, P. P., APPATHURAI, S., HARRIS, M. T., PASQUALI, M., MCKINLEY, G. H. & BASARAN, O. A. 2010 Formation of beads-on-a-string structures during break-up of viscoelastic filaments. *Nat. Phys.* **6** (8), 625–631.

CASTREJÓN-PITA, J. R., MUÑOZ-SÁNCHEZ, B. N., HUTCHINGS, I. M. & CASTREJÓN-PITA, A. A. 2016 Droplet impact onto moving liquids. *J. Fluid Mech.* **809**, 716–725.

CHAN, D. Y. C., KLASEBOER, E. & MANICA, R. 2011 Film drainage and coalescence between deformable drops and bubbles. *Soft Matt.* **7** (6), 2235–2264.

CHARLES, C. E. & MASON, S. G. 1960 The coalescence of liquid drops with flat liquid/liquid interfaces. *J. Colloid Interface Sci.* **15** (3), 236–267.

COUDER, Y., FORT, E., GAUTIER, C.-H. & BOUDAOUD, A. 2005 From bouncing to floating: noncoalescence of drops on a fluid bath. *Phys. Rev. Lett.* **94** (17), 177801.

DAI, B. & LEAL, L. G. 2008 The mechanism of surfactant effects on drop coalescence. *Phys. Fluids* **20** (4), 040802.

DALILI, A., ESMAEELPANAH, J., CHANDRA, S. & MOSTAGHIMI, J. 2017 Coalescence and agglomeration of droplets sprayed on a substrate. *Atomiz. Sprays* **27** (1), 81–94.

DAMIANO, A. P., BRUN, P.-T., HARRIS, D. M., GALEANO-RIOS, C. A. & BUSH, J. W. M. 2016 Surface topography measurements of the bouncing droplet experiment. *Exp. Fluids* **57** (10), 163.

DAVANLOU, A. 2016 The role of liquid properties on lifetime of levitated droplets. *Langmuir* **32** (38), 9736–9742.

DAVIS, D., DRANSFIELD, P. & TAN, A. 1980 The stable floating liquid droplet phenomenon. In *7th Australasian Conference on Hydraulics and Fluid Mechanics 1980: Preprints of Papers*, p. 451. Institution of Engineers, Australia.

DELL'AVERSANA, P., BANAVAR, J. R. & KOPLIK, J. 1996 Suppression of coalescence by shear and temperature gradients. *Phys. Fluids* **8** (1), 15–28.

DENG, N. N., WANG, W., JU, X. J., XIE, R. & CHU, L. Y. 2016 Spontaneous transfer of droplets across microfluidic laminar interfaces. *Lab on a Chip* **16** (22), 4326–4332.

DIJKHUIZEN, W., ROGHAIR, I., ANNALAND, M. V. S. & KUIPERS, J. A. M. 2010 DNS of gas bubbles behaviour using an improved 3D front tracking model—drag force on isolated bubbles and comparison with experiments. *Chem. Engng Sci.* **65** (4), 1415–1426.

DONG, T., WEHELIYE, W. H. & ANGELI, P. 2019 Laser induced fluorescence studies on the distribution of surfactants during drop/interface coalescence. *Phys. Fluids* **31** (1), 012106.

DONG, T., WEHELIYE, W. H., CHAUSSET, P. & ANGELI, P. 2017 An experimental study on the drop/interface partial coalescence with surfactants. *Phys. Fluids* **29** (10), 102101.

DUCHEMIN, L., LISTER, J. R. & LANGE, U. 2005 Static shapes of levitated viscous drops. *J. Fluid Mech.* **533**, 161–170.

ESMAILIZADEH, L. & MESLER, R. 1986 Bubble entrainment with drops. *J. Colloid Interface Sci.* **110** (2), 561–574.

FARHADI, H., RIAHI, S., AYATOLLAHI, S. & AHMADI, H. 2016 Experimental study of nanoparticle-surfactant-stabilized CO_2 foam: stability and mobility control. *Chem. Engng Res. Des.* **111**, 449–460.

FATHI, S., DICKENS, P. & FOUCHAL, F. 2010 Regimes of droplet train impact on a moving surface in an additive manufacturing process. *J. Mater. Process. Technol.* **210** (3), 550–559.

GERI, M., KESHAVARZ, B., MCKINLEY, G. H. & BUSH, J. W. M. 2017 Thermal delay of drop coalescence. *J. Fluid Mech.* **833**, R3.

HAHN, P. S., CHEN, J. D. & SLATTERY, J. C. 1985 Effects of London-van der Waals forces on the thinning and rupture of a dimpled liquid film as a small drop or bubble approaches a fluid–fluid interface. *AlChE J.* **31** (12), 2026–2038.

HALE, J. & AKERS, C. 2016 Deceleration of droplets that glide along the free surface of a bath. *J. Fluid Mech.* **803**, 313–331.

HAMROCK, B. J., SCHMID, S. R. & JACOBSON, B. O. 2004 *Fundamentals of Fluid Film Lubrication*. CRC.

HARTLAND, S., RAMAKRISHNAN, S. & HARTLEY, R. W. 1975 The oscillation of drops and spheres at fluidl iquid interfaces. *Chem. Engng Sci.* **30** (9), 1141–1148.

JAFARI, S. M., ASSADPOOR, E., HE, Y. H. & BHANDARI, B. Re-coalescence of emulsion droplets during high-energy emulsification. *Food Hydrocoll.* **22** (7), 1191–1202.

KAVEHPOUR, H. P. 2015 Coalescence of drops. *Annu. Rev. Fluid Mech.* **47**, 245–268.

KLASEBOER, E., CHEVAILLIER, J. P., GOURDON, C. & MASBERNAT, O. 2000 Film drainage between colliding drops at constant approach velocity: experiments and modeling. *J. Colloid Interface Sci.* **229** (1), 274–285.

KLYUZHIN, I. S., IENNA, F., ROEDER, B., WEXLER, A. & POLLACK, G. H. 2010 Persisting water droplets on water surfaces. *J. Phys. Chem.* B **114** (44), 14020–14027.

LEAL, L. G. 2007 *Advanced Transport Phenomena: Fluid Mechanics and Convective Transport Processes*, vol. 7. Cambridge University Press.

LEE, S., LI, E. Q., MARSTON, J. O., BONITO, A. & THORODDSEN, S. T. 2013 Leaping shampoo glides on a lubricating air layer. *Phys. Rev.* E **87** (6), 061001.

LHUISSIER, H., TAGAWA, Y., TRAN, T. & SUN, C. 2013 Levitation of a drop over a moving surface. *J. Fluid Mech.* **733**, R4.

LI, E. Q., ZHANG, J. M. & THORODDSEN, S. T. 2013 Simple and inexpensive microfluidic devices for the generation of monodisperse multiple emulsions. *J. Micromech. Microengng* **24** (1), 015019.

MOHAMED-KASSIM, Z. & LONGMIRE, E. K. 2003 Drop impact on a liquid–liquid interface. *Phys. Fluids* **15** (11), 3263–3273.

MOHAMED-KASSIM, Z. & LONGMIRE, E. K. 2004 Drop coalescence through a liquid/liquid interface. *Phys. Fluids* **16** (7), 2170–2181.

MOLÁČEK, J. & BUSH, J. W. M. 2013 Drops walking on a vibrating bath: towards a hydrodynamic pilot-wave theory. *J. Fluid Mech.* **727**, 612–647.

MUIJLWIJK, K., COLIJN, I., HARSONO, H., KREBS, T., BERTON-CARABIN, C. & SCHROËN, K. 2017 Coalescence of protein-stabilised emulsions studied with microfluidics. *Food Hydrocoll.* **70**, 96–104.

MURANO, M. & OKUMURA, K. 2018 Bursting dynamics of viscous film without circular symmetry: the effect of confinement. *Phys. Rev. Fluids* **3** (3), 031601.

NAKAYAMA, Y. 2018 *Introduction to Fluid Mechanics*. Butterworth-Heinemann.

NAPOLITANO, L. G., MONTI, R. & RUSSO, G. 1986 Marangoni convection in one-and two-liquids floating zones. *Naturwissenschaften* **73** (7), 352–355.

OLDENZIEL, G., DELFOS, R. & WESTERWEEL, J. 2012 Measurements of liquid film thickness for a droplet at a two-fluid interface. *Phys. Fluids* **24** (2), 022106.

OUDHEUSDEN, B. W. V. 2013 PIV-based pressure measurement. *Meas. Sci. Technol.* **24** (3), 032001.

PIRAT, C., LEBON, L., FRULEUX, A., ROCHE, J. S. & LIMAT, L. 2010 Gyroscopic instability of a drop trapped inside an inclined circular hydraulic jump. *Phys. Rev. Lett.* **105** (8), 084503.

PUCCI, G., HARRIS, D. M., FARIA, L. M. & BUSH, J. W. M. 2018 Walking droplets interacting with single and double slits. *J. Fluid Mech.* **835**, 1136–1156.

REYNOLDS, O. 1881 On drops floating on the surface of water. *Chem. News* **44** (1881), 211.

ROMMEL, W., BLASS, E. & MEON, W. 1993 Plate separators for dispersed liquid–liquid systems: the role of partial coalescence. *Chem. Engng Sci.* **48** (10), 1735–1743.

SAJJADI, S., ZERFA, M. & BROOKS, B. W. 2002 Dynamic behaviour of drops in oil/water/oil dispersions. *Chem. Engng Sci.* **57** (4), 663–675.

SAMBATH, K., GARG, V., THETE, S. S., SUBRAMANI, H. J. & BASARAN, O. A. 2019 Inertial impedance of coalescence during collision of liquid drops. *J. Fluid Mech.* **876**, 449–480.

SAVINO, R., PATERNA, D. & LAPPA, M. 2003 Marangoni flotation of liquid droplets. *J. Fluid Mech.* **479**, 307–326.

SAWAGUCHI, E., MATSUDA, A., HAMA, K., SAITO, M. & TAGAWA, Y. 2019 Droplet levitation over a moving wall with a steady air film. *J. Fluid Mech.* **862**, 261–282.

SÁENZ, P. J., CRISTEA-PLATON, T. & BUSH, J. W. M. 2018 Statistical projection effects in a hydrodynamic pilot-wave system. *Nat. Phys.* **14** (3), 315.

SMITH, M. K. & NEITZEL, G. P. 2006 Multiscale modelling in the numerical computation of isothermal non-wetting. *J. Fluid Mech.* **554**, 67–83.

SREENIVAS, K. R., DE, P. K. & ARAKERI, J. H. 1999 Levitation of a drop over a film flow. *J. Fluid Mech.* **380**, 297–307.

TCHOLAKOVA, S., DENKOV, N. D., IVANOV, I. B. & CAMPBELL, B. 2006 Coalescence stability of emulsions containing globular milk proteins. *Adv. Colloid Interface Sci.* **123**, 259–293.

THORODDSEN, S. T. & MAHADEVAN, L. 1997 Experimental study of coating flows in a partially-filled horizontally rotating cylinder. *Exp. Fluids* **23** (1), 1–13.

VAKARELSKI, I. U., YANG, F., TIAN, Y. S., LI, E. Q., CHAN, D. Y. C. & THORODDSEN, S. T. 2019 Mobile-surface bubbles and droplets coalesce faster but bounce stronger. *Sci. Adv* **5** (10), eaaw4292.

VENKATARAMAN, P., TANG, J. J., FRENKEL, E., MCPHERSON, G. L., HE, J. B., RAGHAVAN, S. R., KOLESNICHENKO, V., BOSE, A. & JOHN, V. T. 2013 Attachment of a hydrophobically modified biopolymer at the oil–water interface in the treatment of oil spills. *ACS Appl. Mater. Interfaces* **5** (9), 3572–3580.

WALKER, J. 1978 *Drops of Liquid Can be Made to Float on the Liquid*. The Amateur Scientist.

YEO, L. Y. & MATAR, O. K. 2003 Hydrodynamic instability of a thin viscous film between two drops. *J. Colloid Interface Sci.* **261** (2), 575–579.

YIANTSIOS, S. G. & DAVIS, R. H. 1990 On the buoyancy-driven motion of a drop towards a rigid surface or a deformable interface. *J. Fluid Mech.* **217**, 547–573.